

Cite this article as: Ding Wanwu, Chen Shihao, Hu Liwen, et al. Hot Deformation Behavior and Microstructural Evolution of ZL270LF Aluminum Alloy[J]. Rare Metal Materials and Engineering, 2023, 52(12): 4086-4098. DOI: 10.12442/j.issn.1002-185X.20230311.

ARTICLE

Hot Deformation Behavior and Microstructural Evolution of ZL270LF Aluminum Alloy

Ding Wanwu^{1,2}, Chen Shihao^{1,2}, Hu Liwen^{1,2}, Zhang Haixia^{1,2}, Yu Haicun^{1,2}, Zhao Wenjun^{1,2}

¹School of Materials Science and Engineering, Lanzhou University of Technology, Lanzhou 730050, China; ²State Key Laboratory of Advanced Processing and Recycling of Nonferrous Metals, Lanzhou University of Technology, Lanzhou 730050, China

Abstract: The hot deformation behavior of ZL270LF aluminum alloy under a strain of 70%, deformation temperatures ranging from 300 °C to 550 °C, and strain rate ranging from 0.01 s⁻¹ to 10 s⁻¹ was studied by hot compression tests. A constitutive equation for flow stress was constructed, and the hot processing map was drawn, thus determining the optimal hot processing region. An electron back scattered diffractometer (EBSD) and a transmission electron microscope (TEM) were used to explore microstructural evolution of the alloy. The results show that the flow stress of ZL270LF Al alloy decreases with increasing deformation temperature and decreasing strain rate. The deformation activation energy is 309.05 kJ/mol, and the optimal processing region is the area where the temperature is from 470 °C to 530 °C and the strain rate is from 0.01 s⁻¹ to 1 s⁻¹. Three different dynamic recrystallization (DRX) mechanisms are involved in the hot deformation process of the alloy, namely continuous dynamic recrystallization (CDRX), discontinuous dynamic recrystallization (DDRX), and geometric dynamic recrystallization (GDRX). Among them, CDRX is the main DRX mechanism of ZL270LF Al alloy.

Key words: ZL270LF aluminum alloy; hot deformation behavior; constitutive equation; dynamic recrystallization; microstructural evolution

Aluminum-copper alloys have been widely applied in aerospace, civil transportation, and architecture due to their advantages including high strength, excellent corrosion resistance, and outstanding mechanical properties^[1-4]. ZL270LF Al alloy, a cast Al-Cu alloy, is one of the representative high-performance Al alloys developed independently by Chinese researchers in recent years. The alloy has potential applications in multiple fields.

ZL270LF Al alloy, with a high alloying degree, high tensile and yield strengths, has a narrow area suitable for hot processing. In the processing process, problems including surface cracks, adiabatic shear bands (ASBs), and non-uniform distribution of grains may occur once inappropriate processing parameters are used^[5-8]. Therefore, it is necessary to study the hot deformation behavior and microstructural evolution of ZL270LF Al alloy. By doing so, appropriate hot processing intervals and desired microstructures can be obtained, thus

further optimizing the performance of plastically worked alloy products^[9-10].

To date, many researchers have performed in-depth research on the hot deformation behavior of Al-Cu alloys under different technological conditions. Yan et al^[11] plotted the processing map of Al-Cu-Li alloys and found that the appropriate hot processing parameters include a temperature from 450 °C to 500 °C and a strain rate from 0.01 s⁻¹ to 0.1 s⁻¹. Nayan et al^[12] plotted the processing map of 2195 Al alloy and found that DRX serves as the main softening mechanism of 2195 Al alloy. In addition, the appropriate processing parameters include a temperature in the range from 400 °C to 450 °C and strain rate in the ranges either from 10⁻² s⁻¹ to 10^{-1.5} s⁻¹ or from 10^{-0.5} s⁻¹ to 10 s⁻¹. Miao et al^[13] investigated the hot deformation behavior and microstructures of AA2070 Al alloy at different temperatures and strain rates and discussed the relationship between activation energy and initial micro-

Received date: May 23, 2023

Foundation item: National Natural Science Foundation of China (52161006); Gansu Provincial Department of Education (2021CYZC-23); Gansu Key Research and Development Program (21YF5GD183, 18YF1GA061); Jiayuguan Science and Technology Planning Project (21-10); China Postdoctoral Science Foundation Project (2019M653896XB)

Corresponding author: Ding Wanwu, Ph.D., Professor, School of Materials Science and Engineering, Lanzhou University of Technology, Lanzhou 730050, P. R. China, E-mail: dingww@lut.edu.cn

Copyright © 2023, Northwest Institute for Nonferrous Metal Research. Published by Science Press. All rights reserved.

structures, thus determining the optimal processing conditions of Al-Li-Cu alloys. Shi et al^[14] revealed the dynamic softening mechanism in the hot deformation process of Al-Zn-Mg-Cu alloys. They considered that dynamic recovery (DRV) is the main low-temperature softening mechanism, while discontinuous dynamic recrystallization (DDRX) and continuous dynamic recrystallization (CDRX) occur in the high-temperature softening process. Although researchers have studied different Al-Cu alloys, the microstructural evolution of ZL270LF Al alloy and its mechanism under different deformation conditions have not, at time of writing, been reported.

The investigation focused on the process of the alloy at different temperatures and strain rates, especially the dynamic recrystallization (DRX) and microstructural evolution of the ZL270LF Al alloy during the hot deformation process. The aim of this study is to provide a theoretical basis for optimizing the hot processing parameters, reducing the production cycle, and improving the efficiency of production of the alloy.

1 Experiment

The experimental material was ZL270LF Al alloy provided by Lanzhou Flight Control Co., Ltd. Table 1 lists the main composition of the alloy. Before hot compression, the alloy was machined into cylindrical samples of $\Phi 10 \text{ mm} \times 15 \text{ mm}$

Table 1 Main composition of ZL270LF Al alloy (wt%)

Cu	Mn	Mg	Si	Ti	Re	Al
4.73	0.777	0.603	0.395	0.191	0.018	Bal.

and then preserved at $565 \text{ }^\circ\text{C}$ for 4 h, followed by homogenization. Hot compression tests were conducted on a Gleeble-3500 hot-working simulator at deformation temperatures of 300, 350, 400, 450, 500, and $550 \text{ }^\circ\text{C}$ and strain rates of 0.01, 0.1, 1, and 10 s^{-1} . In addition, the true strain under compression was 1.2 (deformation with 70% engineering strain). To ensure that the collected experimental data were recorded under uniaxial pressure and to avoid excessive friction between the sample and the pressure head to influence the deformation, lubrication with the addition of graphite flakes at two ends of the sample was applied. In the stage involving an increasing temperature, the sample was heated at $5 \text{ }^\circ\text{C/s}$ to the required experimental temperature. After reaching the corresponding temperature, the sample was preserved for 5 min to eliminate the temperature gradient and then the experiments started. After compression, the sample was water-quenched immediately to retain the deformed microstructures. The experimental data were obtained automatically using the hot-working simulator.

The compressed sample was cut along the compression axis and then mechanically ground, polished, and corroded to prepare the metallographic samples. The microstructures of the sample were observed using an electron backscattered diffractometer (EBSD, EDAX Hikari Plus) and a transmission electron microscope (TEM, FEI Tecnai F30).

2 Results and Discussion

2.1 Microstructures of samples before hot deformation

The microstructure of the ZL270LF aluminum alloy at as-cast state is shown in Fig. 1. Fig. 1a and 1b show the

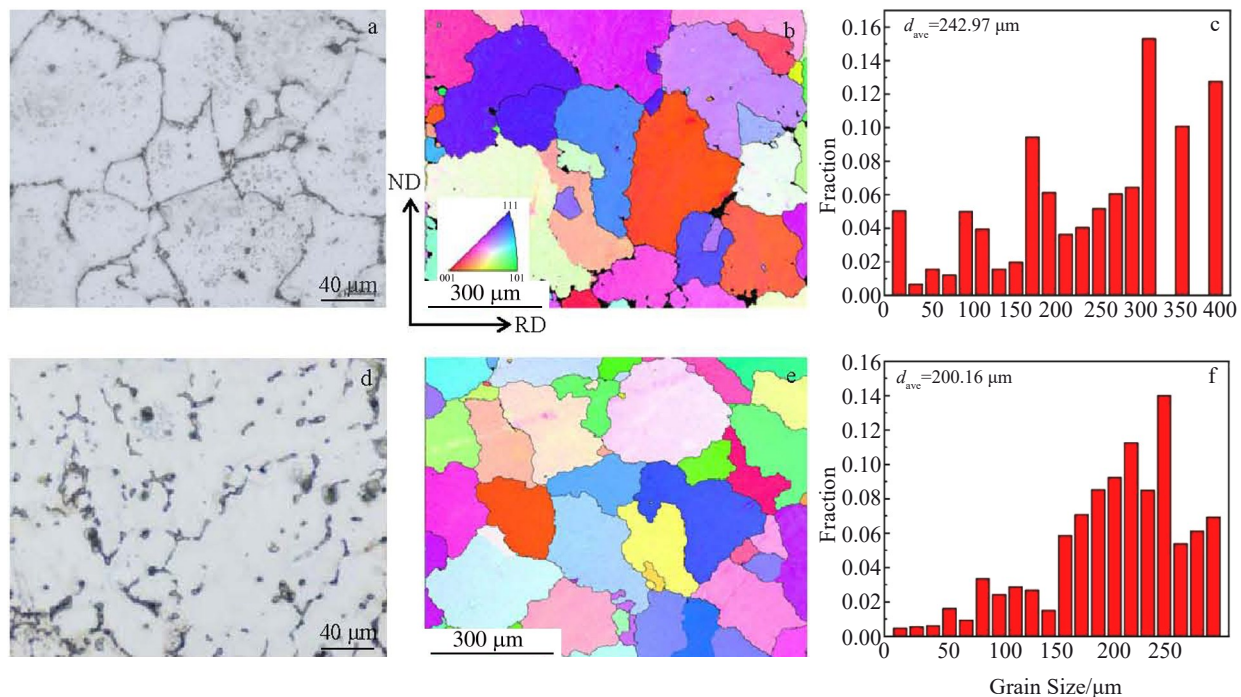


Fig.1 Microstructures (a, d), EBSD maps (b, e), and grain size distributions (c, f) of as-cast ZL270LF Al alloy (a–c) and homogenized ZL270LF Al alloy at $530 \text{ }^\circ\text{C}$ (d–f)

morphologies of the as-cast microstructure, while Fig. 1d and 1e illustrate the homogenized microstructure at 530 °C: the original structure of the alloy primarily consists of equiaxed grains of different sizes. The average grain size of the as-cast ZL270LF aluminum alloy is approximately 242 μm , whereas the average grain size of the alloy after homogenization is around 200 μm . The second phase is transformed from a reticular morphology to a worm-like morphology, resulting in a more uniform distribution of grains and smaller grain size.

2.2 Flow stress

2.2.1 True stress-strain curves

Fig. 2 shows the true stress-true strain curves of ZL270LF aluminum alloy at different deformation temperatures and the strain rate of 0.01, 0.1, 1.0, 10 s^{-1} . As illustrated in Fig. 2, the flow stress curves always rapidly ascend in the initial stage while tend to be stable in the middle and late stages. When the strain exceeds 0.7, the curves rise again. This is because under a large strain, DRV and DRX within the material fail to reach a dynamic equilibrium, leading to flow instability of the alloy. The material undergoes work hardening during the early stages of deformation^[15-16]. As the deformation continues, the strain gradually increases, and the rate of stress increase slows down. After reaching the peak stress, the material enters a stage of dynamic softening, DRX and DRV, and the softening behavior and work hardening reach a dynamic equilibrium within the material, dissipating the accumulated strain energy and numerous dislocations generated during its deformation^[17-18].

Observations of flow stress curves indicate that the peak

stress σ_p at a high strain rate and a low deformation temperature exceeds that at a low strain rate and a high deformation temperature. This is because at a high strain rate, the material does not have enough time to undergo dynamic softening. So it cannot eliminate a large number of formed dislocations. As a result, the work hardening remains dominant. While at a low strain rate, the material has enough time to undergo dynamic softening, so the peak flow stress σ_p is low. The alloy shows high initial energy at a high deformation temperature, which is conducive to the consumption and merging of dislocations in the material, thus leading to the low peak flow stress.

2.2.2 Establishment and analysis of the constitutive equation

The flow stress (σ) is related to the deformation temperature (T), strain (ϵ), and strain rate ($\dot{\epsilon}$) in the hot-deformation process. Their relationships can be expressed by the kinetic equation controlled by heat activation. Such relationships are expressed by the Arrhenius hyperbolic sine function proposed by Sellars and Tegart^[19-20], which includes the deformation temperature and strain activation energy (Q). Meanwhile, the temperature-compensated strain rate Z (the Zener-Hollomon parameter) is given by:

$$Z = \dot{\epsilon} \exp [Q/RT] \quad (1)$$

where R is the gas constant. The strain rate ($\dot{\epsilon}$) varies with the applied stress:

At a low stress (<0.8),

$$\dot{\epsilon} = A_1 \sigma^{n_1} \exp [-Q/RT] \quad (2)$$

At a high stress (>1.2),

$$\dot{\epsilon} = A_2 \exp (\beta \sigma) \exp [-Q/RT] \quad (3)$$

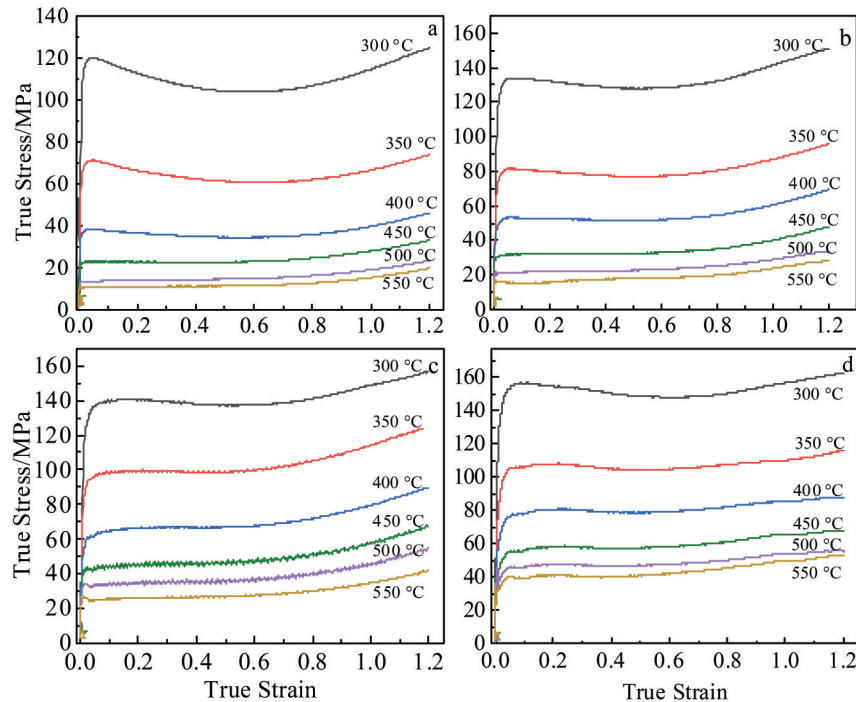


Fig. 2 True stress-true strain curves of ZL270LF Al alloy at different deformation temperatures and the strain rate of 0.01 s^{-1} (a), 0.1 s^{-1} (b), 1 s^{-1} (c), and 10 s^{-1} (d)

At all stresses,

$$\dot{\epsilon} = A [\sinh(\alpha\sigma_p)]^n \exp[-Q/RT] \quad (4)$$

where A , n , and β are constants; α is the parameter related to the stress; R is the ideal gas constant (8.314 J/mol/K). Taking the natural logarithm on both sides of Eq.(1-4):

$$\ln Z = \ln A + n_1 \ln [\sinh(\alpha\sigma)] \quad (5)$$

$$\ln \dot{\epsilon} = \ln A_1 + n_1 \ln \sigma - \frac{Q}{RT} \quad (6)$$

$$\ln \dot{\epsilon} = \ln A_2 + \beta \sigma - \frac{Q}{RT} \quad (7)$$

$$\ln \dot{\epsilon} = \ln A + n \ln [\sinh(\alpha\sigma)] + \beta \sigma - \frac{Q}{RT} \quad (8)$$

Under different conditions, the relationship between $\ln \dot{\epsilon} - \ln \sigma$ and $\ln \dot{\epsilon} - \sigma$ can be fitted through linear regression according to the peak flow stress. The values of n_1 and β can be obtained through averaging.

Manipulation of Eq.(4) gives

$$Q = R \left. \frac{\partial \ln \dot{\epsilon}}{\partial \ln [\sinh(\alpha\sigma)]} \right|_T \left. \frac{\partial \ln [\sinh(\alpha\sigma)]}{\partial (1/T)} \right|_{\dot{\epsilon}} = RnK \quad (9)$$

Fig. 3 shows $\ln \dot{\epsilon} - \ln \sigma$, $\ln \dot{\epsilon} - \sigma$, $\ln \dot{\epsilon} - \ln [\sinh(\alpha\sigma)]$, and $\ln [\sinh(\alpha\sigma)] - 1/T$ relationships. According to Eq.(9), $\ln \dot{\epsilon}$ and $\ln [\sinh(\alpha\sigma)]$ have a linear relationship, so do $\ln [\sinh(\alpha\sigma)]$ and $1/T$, at a fixed strain rate and deformation temperature. By linear regression using the least-squares method, n , n_1 , and the mean average value of β were obtained ($n=6.16$, $n_1=5.11$, and $\beta=0.12$). By substituting these values into Eq.(9), the deformation activation energy Q of ZL270LF Al alloy is obtained to be 309.05 kJ/mol.

Fig. 4b depicts the linear relationship between $\ln Z$ and $\ln[\sinh(\alpha\sigma)]$. Z values at different deformation temperatures and strain rates can be determined by substituting the strain rate $\dot{\epsilon}$ corresponding to different deformation temperatures and

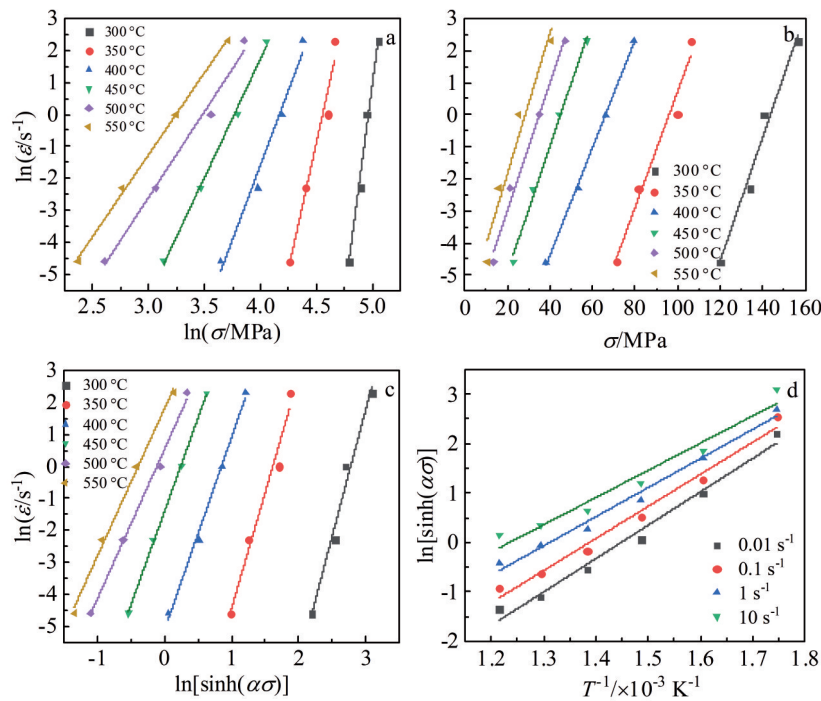


Fig.3 Relationships between $\ln \dot{\epsilon} - \ln \sigma$ (a), $\ln \dot{\epsilon} - \sigma$ (b), $\ln \dot{\epsilon} - \ln [\sinh(\alpha\sigma)]$ (c), and $\ln [\sinh(\alpha\sigma)] - 1/T$ (d)

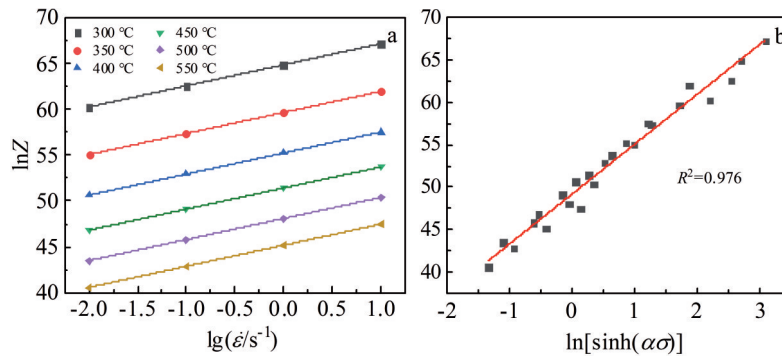


Fig.4 Different $\ln Z$ values at the true strain of 1.2 (a) and linear fitting relationship between $\ln Z$ and $\ln[\sinh(\alpha\sigma)]$ (b)

the calculated deformation activation energy Q into Eq. (1). Based on the linear relationship between $\ln Z$ and $\ln[\sinh(\alpha\sigma)]$, they are also linearly fitted (Fig.4).

Calculation shows that the deformation activation energy of ZL270LF Al alloy is 309.05 kJ/mol. ZL270LF Al alloy has such a high deformation activation energy because it is a rare-earth Al alloy, which contains as much as 0.018% rare-earth elements. Rare-earth elements can promote formation of dispersed granular second phases in the grains. These second phases limit climb and cross-slip of dislocations therein, thus increasing the resistance to deformation. Meanwhile, the high deformation activation energy also indicates that more energy can be accumulated in ZL270LF Al alloy in the hot-deformation process, so DRX becomes the main softening mechanism of the alloy. The presence of multiple DRX phenomena helps to refine the grains and improve the performance of the alloy.

2.2.3 Hot-processing maps

Prasad^[21], Alexander^[22], and Malas^[23] et al plotted hot-processing maps for the dynamic material model (DMM) according to mechanical theory of continuum with large plastic deformation, physical simulation, and irreversible thermodynamics. These maps show the relationship between microstructural evolution and deformation parameters during high-temperature deformation of metals. They can also be used to select reasonable deformation regions of materials and to assess material processing at a specific temperature. DDM maps can be obtained by superimposing safe and unstable regions in the deformation of materials. Hot-processing in the safe regions can, to a large extent, avoid generation of defects including ASBs, hot cracks, and local flow during the processing.

$$P = \sigma \dot{\epsilon} = J + G = \int_0^{\sigma} \dot{\epsilon} d\sigma + \int_0^{\dot{\epsilon}} \sigma d\dot{\epsilon} \quad (10)$$

where P is the total input energy; G is the dissipated energy; J denotes the power dissipation co-content. The proportions of G and J can be described by the strain-rate sensitivity index m .

$$m = \frac{\partial J}{\partial G} = \frac{\dot{\epsilon} \partial \sigma}{\sigma \partial \dot{\epsilon}} = \frac{\dot{\epsilon} \sigma \partial \ln \sigma}{\sigma \dot{\epsilon} \partial \ln \dot{\epsilon}} = \frac{\partial \ln \sigma}{\partial \ln \dot{\epsilon}} \quad (11)$$

Under conditions of constant temperature and strain, the relationship between the stress σ and strain rate $\dot{\epsilon}$ of the material during hot-processing of materials satisfies

$$\sigma = K \dot{\epsilon}^m \quad (12)$$

where K is a constant; m is the strain-rate sensitivity index. So the power dissipation co-content J can be obtained by combining Eq.(10–12), as expressed below:

$$J = \sigma \dot{\epsilon} - \int_0^{\dot{\epsilon}} K \dot{\epsilon}^m = \frac{m}{m+1} \sigma \dot{\epsilon} \quad (0 < m \leq 1) \quad (13)$$

Generally, materials are regarded in the ideal linear dissipation state, when $m = 1$. Under this condition, the power dissipation co-content reaches the maximum J_{\max} :

$$J_{\max} = \frac{1}{2} \sigma \dot{\epsilon} \quad (14)$$

The power dissipation factor η , which can reflect the energy dissipated by the structural evolution of the material under deformation, can be deduced, as follows:

$$\eta = \frac{J}{J_{\max} \frac{2m}{m+1}} \quad (15)$$

In Eq. (16), the function ζ represents the relationship between the deformation temperature and strain rate. Based on the calculated results, the processed maps under different true strains are plotted (Fig.5).

$$\zeta(\dot{\epsilon}) = \frac{\partial \ln \left| \frac{m}{m+1} \right|}{\partial \ln \dot{\epsilon}} + m < 0 \quad (16)$$

Fig.5 shows the hot processing maps of ZL270LF Al alloy at different true strain levels. The instable regions (shadow) during deformation are mainly the regions of low temperature and high strain, where the power dissipation factor η is relatively low. As the strain rises, the instable region gradually moves upward from the lower left corner with large η to the upper left corner with low η . Combining the hot processing map^[24], the optimal processing region of ZL270LF Al alloy is deduced and is approximately located in the region with deformation temperature of 470–530 °C and strain rate of 0.01–0.1 s⁻¹. In order to better understand the softening mechanism of ZL270LF Al alloy during hot deformation, EBSD analysis needs to be performed on deformed microstructures in the safe and unstable regions in the hot processing map to explore the microstructural evolution processes therein.

2.3 Microstructures in deformed ZL270LF Al alloy

2.3.1 Influences of deformation temperature on microstructures

Samples compressed at a strain rate of 0.01 s⁻¹, processing temperatures of 350, 400, 450, and 500 °C, and a strain of 1.2 were selected. They were analyzed by EBSD to reveal influences of different deformation temperatures on the DRV and DRX degrees as well as the microstructures in the materials after plastic deformation.

Fig.6 displays the EBSD inverse pole figure (IPF) maps of ZL270LF Al alloy at the strain rate of 0.01 s⁻¹ and different deformation temperatures. In the figure, the black and yellow lines represent HAGBs (misorientation larger than 15°) and LAGBs (misorientation in the range from 2° to 15°), respectively. Fig.6a–6b indicate that multiple local flow deformation zones develop at narrow and long grain boundaries formed by deformed grains under low-temperature deformation at 350 and 400 °C. These zones are likely to cause flow instability and composed of fine grains. As shown in Fig.6a'–6b', there are numerous yellow lines formed by LAGBs inside the deformed grains, in which sub-boundaries and sub-grains are likely to form^[25]. At a deformation temperature of 350 °C, there are many deformed grains in the alloy, which are also fine. In addition, dense sub-boundaries and sub-grains are present near and inside grain boundaries, indicating the occurrence of DRV of the alloy during low-temperature deformation^[26]. As the deformation temperature is increased to 400 °C, the alloy begins to undergo DRX, during which small DDRX grains begin to appear at jagged initial deformed grains and grain boundaries. As illustrated in Fig.6c–6d, the number of deformed grains and the deformation of the alloy

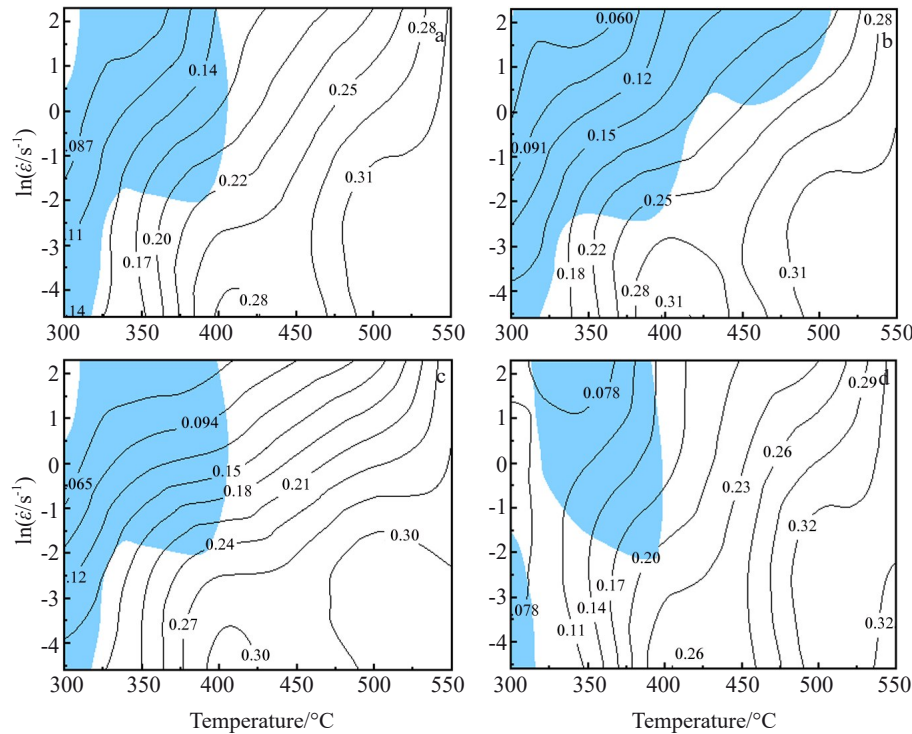


Fig.5 Hot-processing maps of ZL270LF Al alloy at different true strain levels: (a) $\varepsilon=0.3$, (b) $\varepsilon=0.7$, (c) $\varepsilon=1.0$, and (d) $\varepsilon=1.2$

decrease and the grains become equiaxial with increasing the deformation temperature to 450 and 500 °C. As shown in Fig.6c'–6d', sub-boundaries and sub-grains in the alloy decline in number under such conditions. Under the high-temperature deformation condition, grain boundaries move faster and lots of dislocations are rearranged and annihilated through slip, climb, and cross-slip. As a result, the number of LAGBs decreases while that of HAGBs increases and the grain boundaries become clearer. CDRX is likely to occur at these grain boundaries, finally forming new recrystallized grains.

Changes in the distribution of grain boundary misorientations of ZL270LF Al alloy at the strain rate of 0.01 s⁻¹ and different deformation temperatures are illustrated in Fig.7. As the hot-compression temperature of ZL270LF Al alloy rises from 350 °C to 400 °C, the average grain boundary misorientation reduces from 19.759° to 15.35° and the fraction of LAGBs enlarges from 59.59% to 69.12%. This indicates that lots of LAGBs are generated in the hot-deformation process and the reduction of grain boundary misorientations is related to the disappearance and rapid movement of high-energy sub-boundaries in the growth of sub-grains. As the hot compression temperature is increased from 450 °C to 500 °C, the average grain boundary misorientation of ZL270LF Al alloy increases from 23.93° to 26.95° and the fraction of LAGBs decreases from 49.69% to 39.76%. This suggests that sub-boundaries have the increased energy and migrate for a longer time with increasing deformation temperature, which can further activate the recrystallization process in the alloy.

2.3.2 Influences of strain rate on microstructures

The strain rate also affects the recovery and recrystallization of materials after plastic deformation. The samples at the processing temperature of 450 °C and strain rates of 0.01, 0.1, 1, and 10 s⁻¹ were selected to characterize their microstructural evolution and distribution of grain boundary misorientations using EBSD.

Fig.8 illustrates the EBSD IPF maps of ZL270LF Al alloy at the deformation temperature of 450 °C and different strain rates. As shown in Fig.8a–8d, grains are flattened under the compressive force and the chromatic aberration inside deformed grains is a result of the misorientation between numerous sub-grains. Fig.8a demonstrates that at the strain rate of 0.01 s⁻¹, deformed grains are large, have clear boundaries, and are in the equiaxial shape. Fig.8a' demonstrates that there are a small number of relatively large sub-grains composed of LAGBs in deformed grains. As the compression continues, DRX begins and sub-grains merge and grow to form new sub-grains. In addition, LAGBs merge to HAGBs. HAGBs are also the site of the occurrence of DRX. Therefore, compared with grains at a high strain rate, grains at a low strain rate are large and equiaxial in shape. As shown in Fig.8b, when the strain rate is increased to 0.1 s⁻¹, the deformed microstructures become fibrous with a low length-to-width ratio, grains are severely deformed, and grain boundaries become jagged. The white box in Fig.8b' indicates that many fine recrystallized grains exist along the grain boundaries. This is because many dislocations at grain boundaries are tangled to form regions of high dislocation density, which are likely to promote the formation of DDRX.

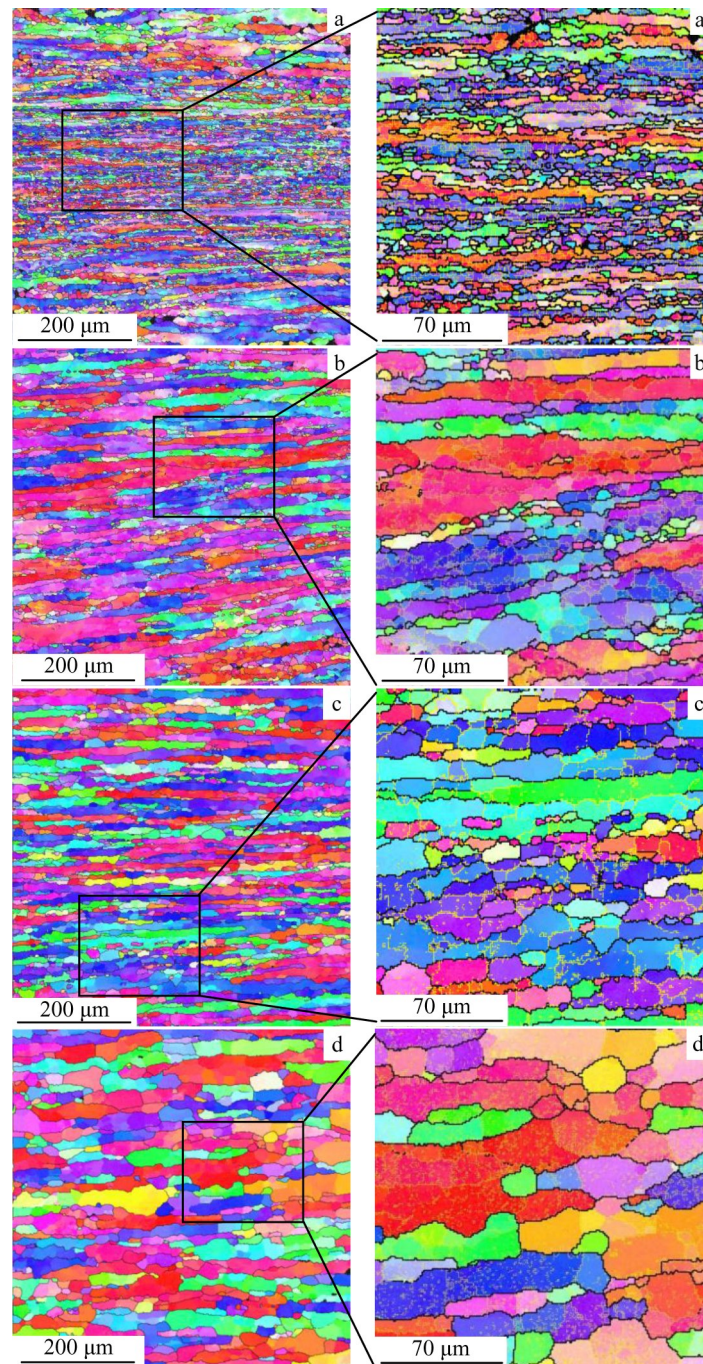


Fig.6 EBSD IPF maps of ZL270LF Al alloy at the strain rate of 0.01 s^{-1} and different deformation temperatures: (a, a') $350 \text{ }^{\circ}\text{C}$, (b, b') $400 \text{ }^{\circ}\text{C}$, (c, c') $450 \text{ }^{\circ}\text{C}$, and (d, d') $500 \text{ }^{\circ}\text{C}$

As shown in Fig. 8c, grain boundaries become more jagged and the increase in fine grains becomes more apparent when the strain rate increases to 1 s^{-1} . Fig. 8c' shows that many CDRX grains similar to the pink grains in the white box and another type of CDRX grains are accumulated at grain boundaries. As displayed in Fig. 8d, when the strain rate is increased to 10 s^{-1} , many fine grains appear and dislocations in grains are tangled and become denser. Geometric dynamic recrystallization (GDRX) grains easily form in the plastic deformation process of the alloy and those with high stacking fault energy can be observed in the white box in Fig.8d^[25].

These results show that the strain rate significantly influences the DRV and DRX of the material in the plastic deformation process. The appearance of multiple DRX mechanisms allows distribution of many small sub-grains in deformed grains. At a low strain rate, grains have enough time to nucleate and to grow, resulting in a high degree of DRX, a reduction in the number of deformed grains, and clearer grain boundaries. At a high strain rate, grains do not have enough time to nucleate and to grow, so DRV and DRX are not completely realized and there are many small deformed grains in the alloy.

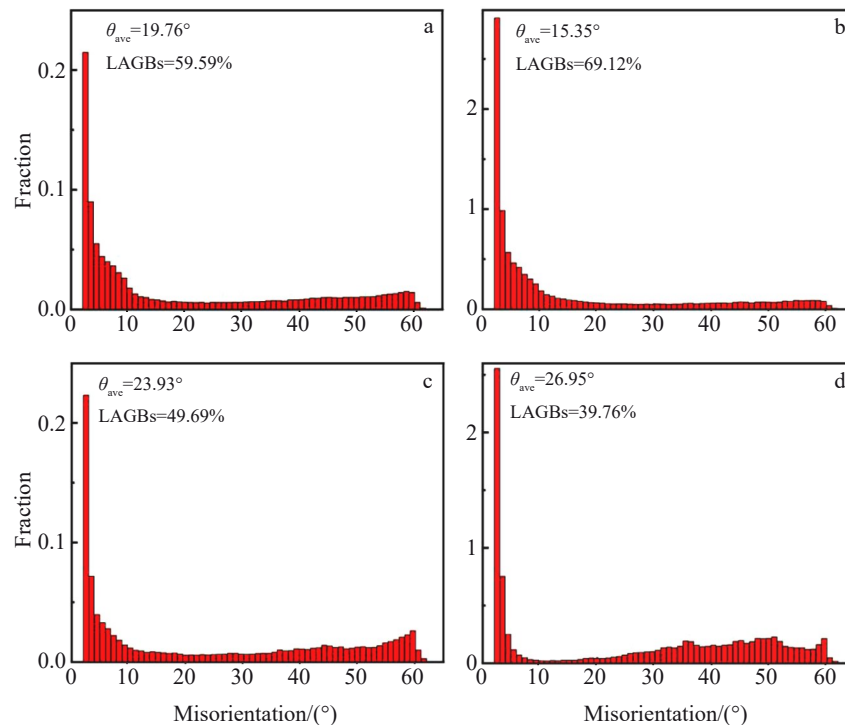


Fig.7 Changes in the distribution of grain boundary misorientations of ZL270LF Al alloy at the strain rate of 0.01 s^{-1} and different deformation temperatures: (a) 350 °C, (b) 400 °C, (c) 450 °C, and (d) 500 °C

Fig.9 shows changes in the distribution of grain boundary misorientations of ZL270LF Al alloy at the deformation temperature of 450 °C and different strain rates. As the strain rate is increased, the average misorientation of the alloy firstly decreases, and then increases while the fraction of LAGBs increases, and then decreases. This is because as the strain rate is increased from 0.01 s^{-1} to 10 s^{-1} , HAGBs gradually become LAGBs. This happens because the dislocation multiplication rate induced by work hardening is higher than that induced by dynamic softening mechanism. So the fraction of LAGBs decreases and the average misorientation increases.

Fig. 10 shows the distributions of recrystallized grains in deformed samples, statistical diagrams for the degree of recrystallization, and statistical diagrams for grain size. Blue, yellow, and red areas in the figures represent the recrystallized, sub-structured, and deformed grains, respectively. As illustrated in Fig.10a (the unstable region of 350 °C and 0.01 s^{-1}), the deformed samples in this region exhibit a lower degree of recrystallization, due to the lower deformation temperature. The red-colored deformed grains and yellow-colored sub-structures are more predominant, and the grains are smaller. Conversely, in Fig.10d (the safe region of 500 °C and 0.01 s^{-1}), those samples deformed at higher temperatures show a dominant blue-colored region of recrystallization, indicating larger grains.

2.3.3 DRX mechanism

Fig. 11 shows the TEM images and EBSD maps of typical recrystallized microstructures in ZL270LF Al alloy. CDRX microstructures in grains are displayed in Fig. 11a and 11b.

The grains contain lots of dislocation cells formed by many dislocation tangles represented by the yellow dotted lines of different sizes. These dislocation cells, as nucleation sites, form CDRX grains (Fig. 11c). Fig. 11d and 11e show CDRX grains at grain boundaries, where dislocation cells formed by accumulation of dislocations indicated by yellow dotted lines are observed. These dislocation cells interact with LAGBs at the original grain boundaries to form CDRX grains in Fig. 11f. Fig. 11g and 11h illustrate DDRX grains. The DDRX mechanism is concentrated at grain boundaries and it results in bulges of grain boundaries, so the dislocation density at bulging boundaries is apparently larger than that at straight grain boundaries. As a result, grain boundaries bulge to form dislocation walls, as shown in the yellow elliptic region. The regions near DDRX exhibit local accumulation of many dislocations and show a high dislocation density. Finally, a train of DDRX grains (Fig. 11i) is formed in these regions. Fig. 11j and 11k show GDRX grains, which are present inside grains and occur mainly under large strain, causing sub-grains to form within the grains and exhibiting stacked morphologies in a form akin to a brick wall. The microstructures are displayed in Fig. 11l.

Two different CDRX mechanisms are shown in Fig. 12a and 12b, which display two processes of formation of CDRX grains. Fig. 12a shows the CDRX formation process in the grains. In the plastic deformation process, DRV causes dislocations to move in grains, thus forming regions of high dislocation density. In these regions, dislocations are tangled and combined with dislocation cells and LAGBs. Thereafter,

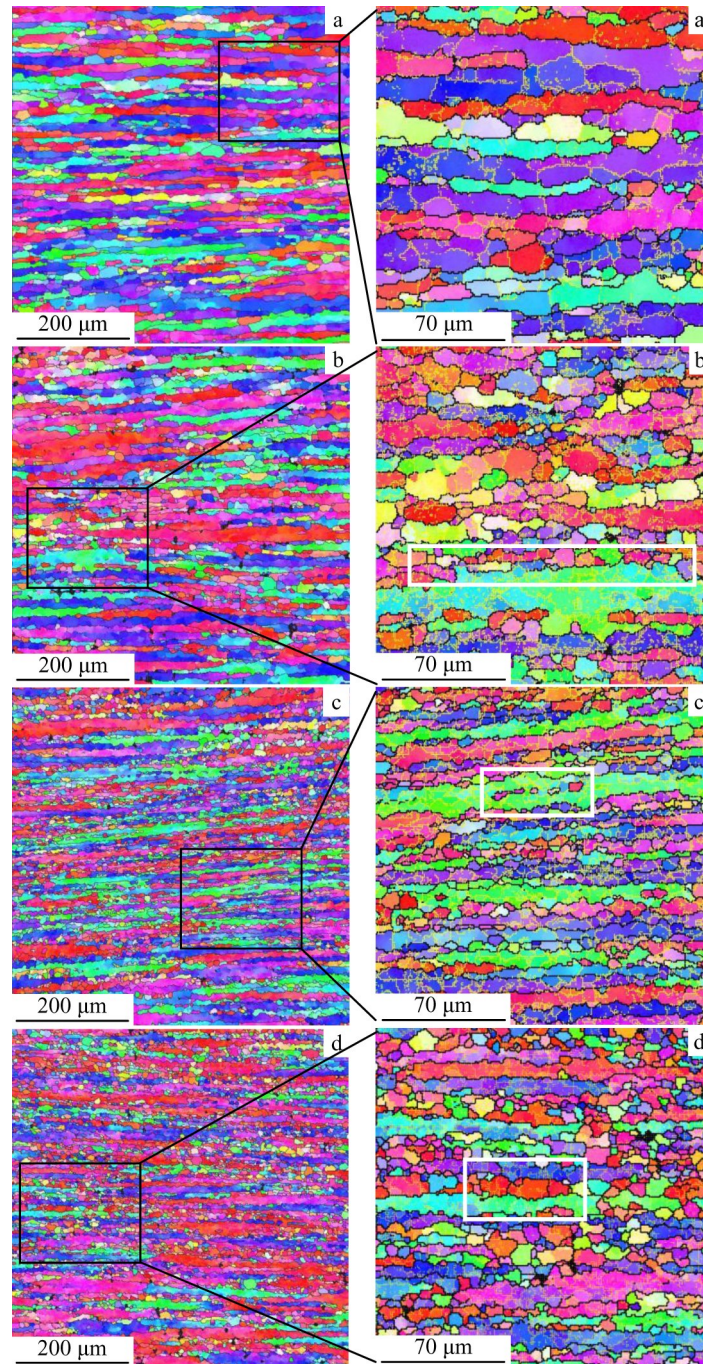


Fig.8 EBSD IPFs maps of ZL270LF Al alloy at deformation temperature of 450 °C and different strain rates: (a, a') 0.01 s⁻¹, (b, b') 0.1 s⁻¹, (c, c') 1 s⁻¹, and (d, d') 10 s⁻¹

sub-grains form at dislocation cells and LAGBs. So multiple sub-grains are formed within the large grains. As the deformation continues, sub-grain rotation (SGR) occurs, finally forming multiple CDRX grains with different misorientations. Fig. 12b illustrates the generation process of CDRX grains at the original grain boundaries ($>15^\circ$). The high stacking fault energy of Al alloy facilitates DRV in the plastic deformation process, which consumes dislocations at grain boundaries and decreases the dislocation density, so these grain boundaries cannot bulge outwards. However, many unconsumed dislocations are still accumulated at grain

boundaries, forming dislocation cells and LAGBs. These LAGBs interact with original grain boundaries via SGR, thus forming new CDRX grains. Therefore, CDRX can occur either inside original grains or at original grain boundaries.

Fig. 12c shows the DDRX mechanism in the plastic deformation process. The original grain boundaries in the plastic deformation process hinder dislocation movement, so dislocations are accumulated at grain boundaries to form regions of high dislocation density, which allow storage of much energy. When the energy is accumulated to a certain extent, grain boundaries move to regions of high dislocation

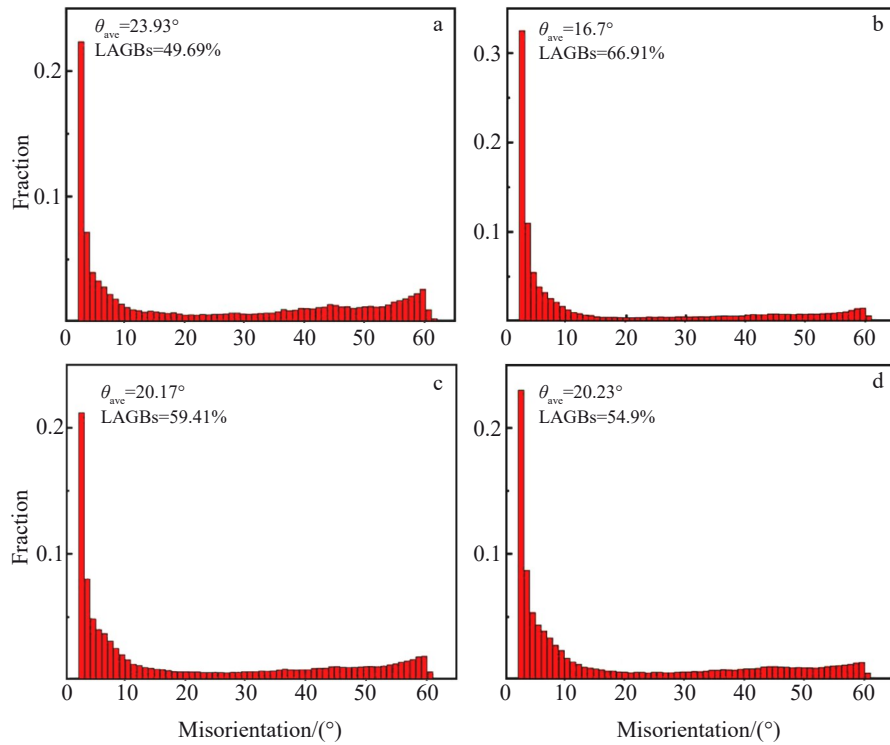


Fig.9 Changes in the distribution of grain boundary misorientations of ZL270LF Al alloy at the deformation temperature of 450 °C and different strain rates: (a) 0.01 s⁻¹, (b) 0.1 s⁻¹, (c) 1 s⁻¹, and (d) 10 s⁻¹

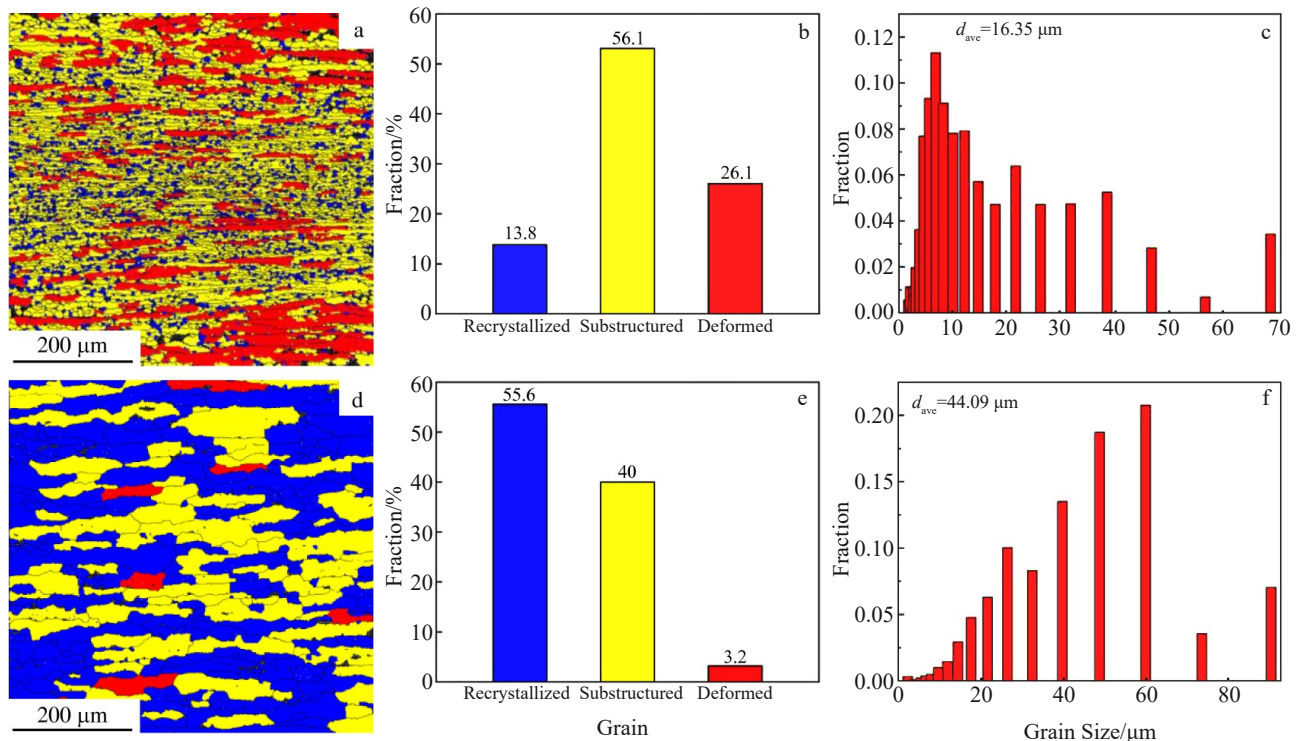


Fig.10 GOS distributions of deformed samples (a, d), statistical diagrams for volume fractions of recrystallized grains (b, e), and grain size distribution (c, f): (a–c) unstable region (350 °C, 0.01 s⁻¹) and (d–f) safe region (500 °C, 0.01 s⁻¹)

density, bulge, and cause local accumulation of dislocations and formation of dislocation walls (the yellow elliptic region

in Fig.11c). Dislocation cells and LAGBs are generated in the regions of high dislocation density at bulging boundaries. The

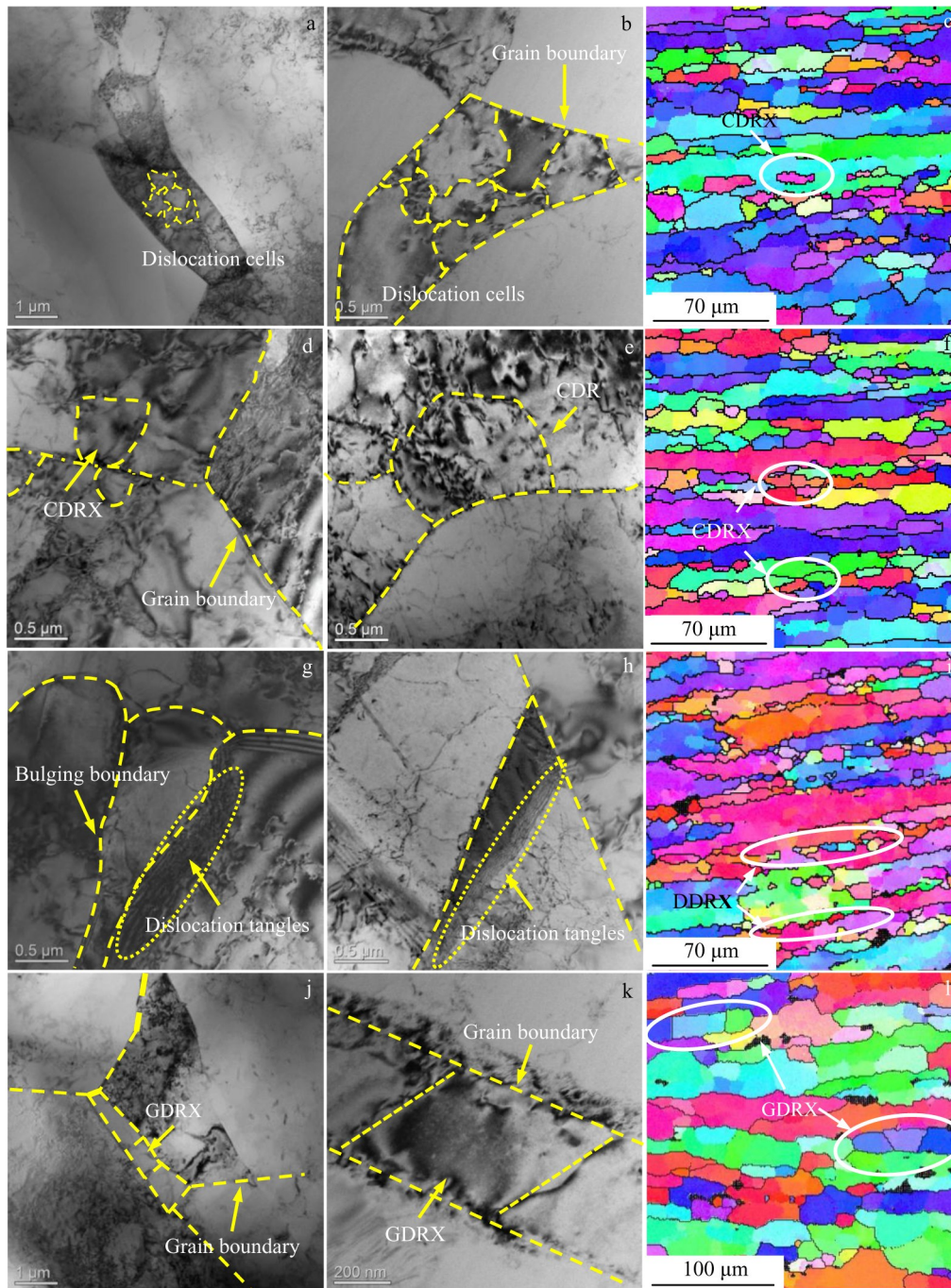


Fig.11 TEM images and EBSD maps of typical recrystallized microstructures in ZL270LF Al alloy: (a–f) CDRX, (g–i) DDRX, and (j–l) GDRX

LAGBs and dislocation cells form sub-grains, which interact to form sub-boundaries and continue to absorb dislocations at bulging boundaries, forming HAGBs. Finally, DDRX grains nucleate and grow in these regions.

Fig. 12d shows the GDRX mechanism in the plastic deformation process. It can be seen from Fig. 12d that grains are under stress in the plastic deformation process, and the spacing between two HAGBs decreases rapidly. Dentate dislocations appear in the grains; as the deformation continues and the spacing between two HAGBs narrows to

about two times as long as the diameter of the sub-grains, these dislocations contact with each other and pinch off the sub-grains to form new sub-grains. As the deformation continues, these newly-formed sub-grains grow to generate new GDRX grains. The nucleation of GDRX grains resembles that of CDRX grains, while GDRX is a process that sub-boundaries generated by deformation evolve to grain boundaries, in which nucleation of new grains is not involved.

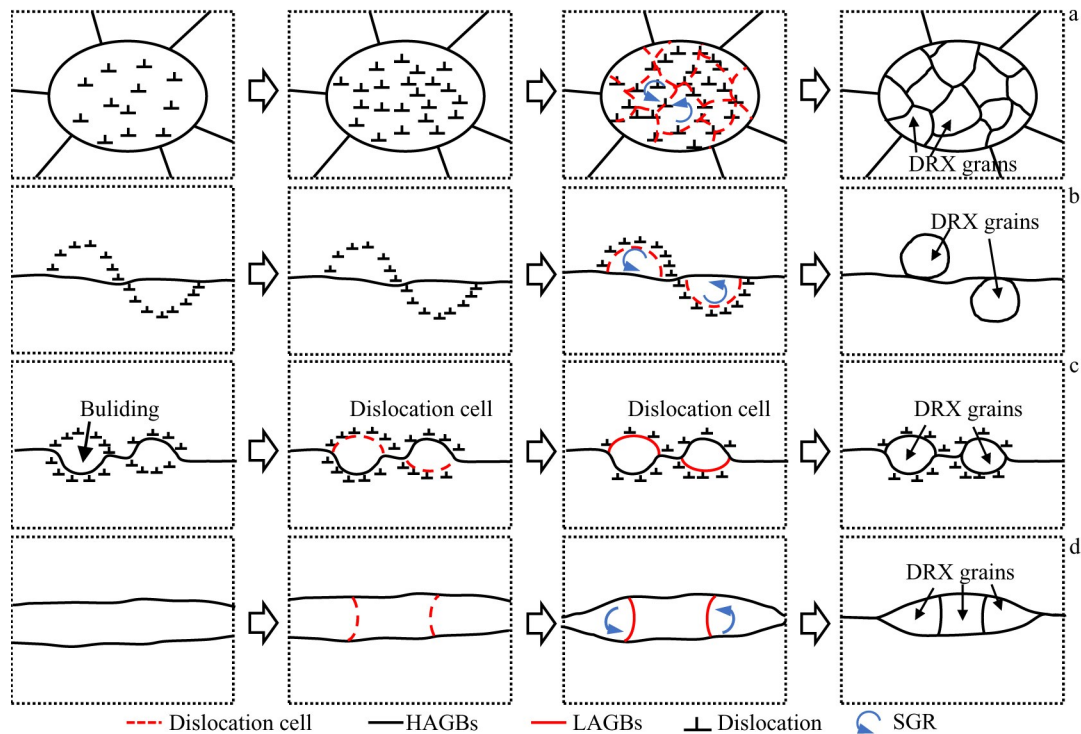


Fig.12 DRX mechanisms in the hot-deformation process of ZL270LF Al alloy: (a–b) CDRX, (c) DDRX, and (d) GDRX

3 Conclusions

1) The flow stress on ZL270LF Al alloy in the hot-deformation process is sensitive to strain, strain rate, and deformation temperature. It decreases with increasing deformation temperature and decreasing strain rate. The flow stress stabilizes after reaching the peak, and plastic instability causes the true stress-true strain curves to rise under high strain in the late stage of deformation.

2) The deformation activation energy of ZL270LF Al alloy is 309.05 kJ/mol. In the hot-processing map, the optimal processing conditions of the alloy are deformation temperatures of 470–530 °C and strain rates of 0.01–0.1 s⁻¹.

3) Three DRX mechanisms (CDRX, DDRX, and GDRX) occur in the hot-deformation process of ZL270LF Al alloy. As the deformation temperature is increased, DRV and DRX occur. The strain rate affects the DRX mechanisms of ZL270LF Al alloy. At a high strain rate, work hardening is apparent and DDRX is the predominant mechanism, while GDRX is also likely to occur. As the strain rate decreases, CDRX predominates.

References

- Li Shujian, Zhan Lihua, Chen Rong et al. *Rare Metal Materials and Engineering*[J], 2016, 45(9): 2282
- Mondol S, Bansal U, Dhanalakshmi P et al. *Journal of Alloys and Compounds*[J], 2022, 921: 166 136
- Guo Youjie, Li Jinfeng, Lu Dinding et al. *Journal of Materials Engineering and Performance*[J], 2021, 30: 2743
- Zhuo Xiaoran, Zhang Quan, Liu Huan et al. *Journal of Alloys and Compounds*[J], 2022, 899: 166 321
- Cao Lingfei, Liao Bin, Wu Xiaodong et al. *Crystals*[J], 2020, 10: 416
- Zhang Huiping, Huang Liang, Wang Zeyu et al. *Rare Metal Materials and Engineering*[J], 2022, 51(7): 2560
- Zhu Xinjie, Fan Qunbo, Wang Duoduo et al. *Scripta Materialia*[J], 2022, 206: 114 229
- Zhao Qiang, Chen Wwen, Lin Jun et al. *International Journal of Material Forming*[J], 2019, 1: 293
- Yu Weichen, Li Hongying, Du Rong et al. *Materials Characterization*[J], 2018, 145: 5364
- Huang Xiaomin, Zang Yong, Guan Ben. *Rare Metal Materials and Engineering*[J], 2022, 51(12): 4745
- Yan Lizhan, Zhang Yongan, Xiong Baiqiang et al. *Materials Science Forum*[C]. Qingdao: Trans Tech Publications Ltd, 2016: 575
- Nayan N, Murty S V S N, ChhanganI S et al. *Journal of Alloys and Compounds*[J], 2017, 723: 548
- Miao Jiashi, Sutton Scott, Luo AlanA. *Materials Science and Engineering A*[J], 2020, 777: 139 048
- Shi Cangji, Lai Jing, Chen X Grant. *Materials*[J], 2014, 7(1): 244
- Sellars C M, McTeagart W J. *Acta Metallurgica*[J], 1966, 14(9): 1136
- Yao Jinjin, Zhang Di, Zhang Jishan. *Rare Metal Materials and Engineering*[J], 2022, 51(6): 2046
- Ding Wanwu, Liu Xiaoxiong, Zhao Xiaoyan et al. *Materials*[J], 2020, 13(19): 4244

- 18 Xu Yike, Huang Liang, Wang Zeyu et al. *Rare Metal Materials and Engineering*[J], 2022, 51(8): 2963
- 19 Deng Lei, Zhuang Haidong, Li Guoai et al. *Transactions of Nonferrous Metals Society of China*[J], 2022, 32(7): 2150
- 20 Su Yu, Kong Fantao, You Fenghai et al. *Vacuum*[J], 2020, 173: 109 135
- 21 Prasad Y V R K, Gegel H L, Doraivelu S M et al. *Metallurgical Transactions A*[J], 1984, 15(10): 1883
- 22 Alexander J M. *Modelling of Hot Deformation of Steels*[M]. Berlin: Springer Verlag, 1989: 105
- 23 Malas J C, Seetharaman V. *JOM*[J], 1992, 44(6): 814
- 24 Su Xin, Shen Shanzhong, Xu Jibo et al. *Rare Metal Materials and Engineering*[J], 2022, 51(3): 850
- 25 Liao Bin, Cao Lingfei, Wu Xiaodong et al. *Materials*[J], 2019, 12(2): 311
- 26 Liu Shuhui, Pan Qinglin, Li Mengjia et al. *Materials & Design*[J], 2019, 184: 108 181

ZL270LF 铝合金的热变形行为与组织演变

丁万武^{1,2}, 陈世豪^{1,2}, 胡立雯^{1,2}, 张海霞^{1,2}, 余海存^{1,2}, 赵文军^{1,2}

(1. 兰州理工大学 材料科学与工程学院, 甘肃 兰州 730050)

(2. 兰州理工大学 省部共建有色金属先进加工与再利用国家重点实验室, 甘肃 兰州 730050)

摘要: 通过热压缩实验研究了 ZL270LF 铝合金在变形量为 70%, 温度为 300~550 °C, 应变速率为 0.01~10 s⁻¹ 范围的热变形行为, 建立了流变应力本构方程模型, 绘制出了二维热加工图, 确定了最佳热加工区域, 采用电子背散射衍射 (EBSD) 和透射电子显微镜 (TEM) 技术研究了该合金的组织演变规律。结果表明: ZL270LF 铝合金的流变应力随变形温度的升高和应变速率的降低而降低, 热变形激活能为 309.05 kJ/mol, 最优热加工区为温度 470~530 °C、应变速率为 0.01~1 s⁻¹。该合金在热变形过程中存在 3 种不同的 DRX 机制, 即连续动态再结晶 (CDRX)、不连续动态再结晶 (DDRX) 和几何动态再结晶 (GDRX), 其中 CDRX 是 ZL270LF 铝合金动态再结晶的主要机制。

关键词: ZL270LF 铝合金; 热变形行为; 本构方程; 动态再结晶; 组织演变

作者简介: 丁万武, 男, 1979 年生, 博士, 研究员, 兰州理工大学材料科学与工程学院, 甘肃 兰州 730050, E-mail: dingww@lut.edu.cn